Negative feedback contributes to the stochastic expression of the interferon-β gene in virus-triggered type I interferon signaling pathways

Wei Zhang [a,b], Tianhai Tian [c], Xiufen Zou [a,*]

[a] *School of Mathematics and Statistics, Wuhan University, Wuhan 430072, China*
[b] *School of Sciences, East China Jiaotong University, Nanchang 330013, China*
[c] *School of Mathematical Science, Monash University, Melbourne Vic 3800, Australia*

ARTICLE INFO

ABSTRACT

Type I interferon (IFN) signaling pathways play an essential role in the defense against early viral infections; however, the diverse and intricate molecular mechanisms of virus-triggered type I IFN responses are still poorly understood. In this study, we analyzed and compared two classes of models i.e., deterministic ordinary differential equations (ODEs) and stochastic models to elucidate the dynamics and stochasticity of type I IFN signaling pathways. Bifurcation analysis based on an ODE model reveals that the system exhibits a bistable switch and a one-way switch at high or low levels when the strengths of the negative and positive feedbacks are tuned. Furthermore, we compared the stochastic simulation results under the Master and Langevin equations. Both of the stochastic equations generate the bistable switch phenomenon, and the distance between two stable states are smaller than normal under the simulation of the Langevin equation. The quantitative computations also show that a moderate ratio between positive and negative feedback strengths is required to ensure a reliable switch between the different IFN concentrations that regulate the immune response. Moreover, we propose a multi-state stochastic model based on the above deterministic model to describe the multi-cellular system coupled with the diffusion of IFNs. The perturbation and inhibition analysis showed that the positive feedback, as well as noises, has little effect on the stochastic expression of IFNs, but the negative feedback of ISG56 on the activation of IRF7 has a great influence on IFN stochastic expression. Together, these results reveal that positive feedback stabilizes IFN gene expression, and negative feedback may be the main contribution to the stochastic expression of the IFN gene in the virus-triggered type I IFN response. These findings will provide new insight into the molecular mechanisms of virus-triggered type I IFN signaling pathways.

1. Introduction

The innate immune response is the first line of defense against microbial infections in both insects and mammals [1–3]. The type-I interferon (IFN) system provides a powerful defense against viral infections in the early stage and has been widely studied in the recent years [4,5].

Recently, the stochastic expression of IFNs in infected cells was reported experimentally [6,7]. The biochemical studies suggested that stochastic IFN induction may result from the cellular heterogeneity in the expression of the viral sensor RIG-1 and activities of the limiting components at every level of the virus induction process, including viral replication and expression, the sensing of viral RNA by host factors and the levels of activated transcription factors in the virus-triggered type-I IFN signaling pathways [8,9]. Although several quantitative studies have simulated the dynamics of these biological processes at the cell-population level [10–14] and considered the influences of cell-to-cell variability [15], the detailed stochastic mechanism underlying the antiviral response remains poorly understood due to the diverse and intricate mechanisms.

Systematic analysis of the innate immune response has provided important insights into the mechanism of maintaining the delicate balance between resistance to infection and viral diseases [16,17]. In our previous work, we developed an ordinary-differential-equation (ODE) model and a simplified delayed model of the virus-triggered type I IFN signaling pathways, that are mainly focused on qualitative dynamical analysis of these signaling pathways [18–20]. However, the detailed feedback regulatory mechanisms, as well as the stochasticity underlying the signaling transmission and gene expression, have not been considered.

In this study, we first developed a simplified deterministic computational model of the biochemical pathways that regulate the

* Corresponding author. Tel.: +862768752958.
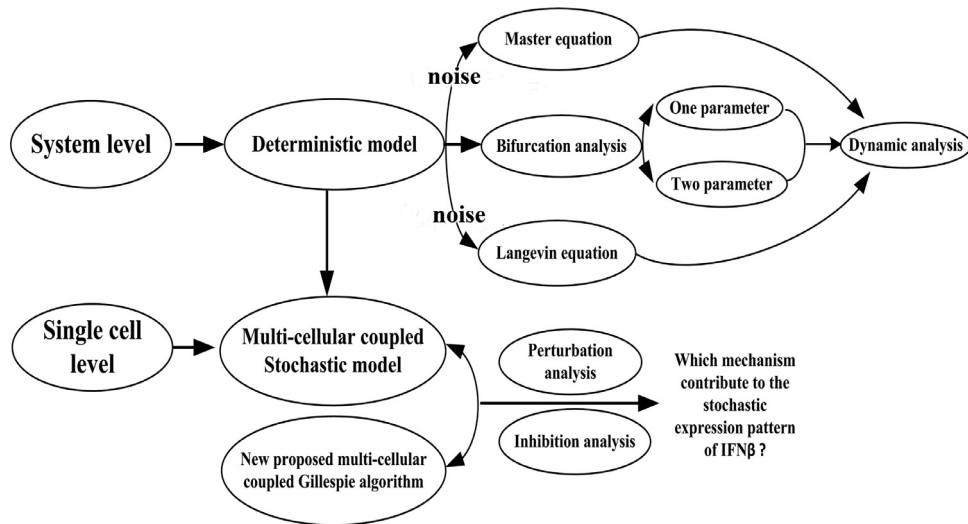 *E-mail address:* xfzou@whu.edu.cn, zouxiufen@yahoo.com (X. Zou).
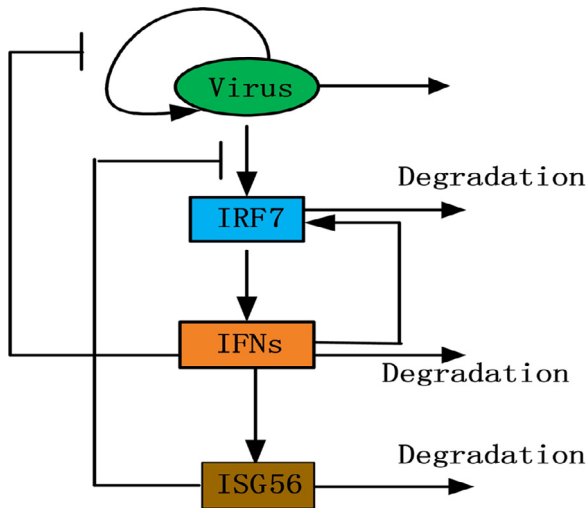
Fig. 1. The workflow of this study.

Fig. 2. (Color online.) A simplified reaction scheme considered in the mathematical model. The core transcriptional circuit underlying the virus-triggered type I IFN signaling pathway.

antiviral program, with particular emphasis on the quantitative bifurcation analysis of the system-level mechanisms underlying this process. Next, we performed stochastic simulation of the system based on the concern of noise underlying the dynamic antiviral processes using the Master and Langevin equations.

To gain insight into the complicated dynamic processes at the multi-cell level and the stochastic expression mechanism underlying the innate immune system, we built a new multi-state stochastic model based on the core deterministic model and conducted perturbation and inhibition analysis. These models and simulation results would be used to investigate the inner mechanisms for the innate immune response. The entire workflow of this study is depicted in Fig. 1.

2. Models and methods

2.1. The core transcriptional circuit underlying the virus-triggered type I IFN signaling pathway

In response to viral infection, dsRNA interacts with the RNA-helicase domain of RIG-1 or MAD5 that serves as cytoplasmic viral RNA sensors [21,22]. The viral RNA sensors transmit signals to the downstream adaptor protein VISA (also known as IPS-1, MAVS, and Cardif). The adaptor protein VISA interacts with MITA and then activates TBK1. Activated TBK1 leads to the phosphorylation of IFN-regulatory factor 3 (IRF3) and IRF7. The activated IRF3 and IRF7 form homo-or heterodimers and are translocated to the nucleus to trigger IFN mRNA induction, leading to the production of type I IFNs [23–26]. Type I IFNs induce the transcription of IFN-stimulated gene factor 3(ISGF3) [27,28], which translocates to the nucleus and induces the transcription of the IRF7 and ISG56 genes. The newly synthesized IRF7 leads to the expression of the IFNβ gene to form an IFNβ-IRF7-IFNβ positive feedback loop and accelerate the induction of type I IFN genes during the host antiviral response [29,30]. The induced ISG56 disrupts the interaction of MITA with VISA or TBK1, leading to the inhibition of virus-induced IRF activation, IFNβ expression and cellular antiviral responses [31]. The IFN-induced antiviral components inhibit virus replication by targeting the viral RNA. In this study, the core transcriptional circuit underlying the virus-triggered type I IFN signaling pathway is depicted in Fig. 2 and involves four main components: Virus, IRF7, IFNβ, and ISG56.

2.2. A deterministic ODE model and non dimensionalization

Based on the simplified reaction diagram shown in Fig. 2, we considered the core circuit that consists of coupled double-negative feedback loops and a positive feedback loop involving four main components Virus, IRF7p, IFNβ and ISG56. The model of circuit network is based on the previous model developed by Zhang et al. [19]. In mouse cells, NF-κB is required only at the early stage when the level of activated IRF3 is low but is not required for the maximum levels of IFNβ late during induction [32]. The main contribution of the type I IFN antiviral system is that IRF7– IFN is involved in positive feedback, and the full induction of type I IFN genes is required for the IRF7 positive feedback [30,31]. To consider the main features of the system, in this study, we selected four main components virus, IRF7, IFNβ, and ISG56 in the circuit. The detailed descriptions of the mathematical modeling are given as follows:

Generally, the concentration of reactant X_i that changes over time can be described by an ordinary differential equation (ODE) [33].

$$\frac{d[X_i]}{dt} = \sum v_{i\,\text{production}} - \sum v_{i\,\text{consumption}}$$

where $v_{i\,\text{production}}$ and $v_{i\,\text{consumption}}$ represent the production rate and consumption rate of reactant X_i, respectively. The derivation of these functions occurs according to the following rules:

(1) The dynamics of the activation, phosphorylation and degradation of the four components following the law of mass action i.e., the activation rates and degradation rates are linearly proportional to their concentrations [34].

(2) The positive and negative feedbacks are represented using Hill functions [35].

The mathematical model of the core circuit network is developed as follows:

$$\frac{\mathrm{d}[V]}{\mathrm{d}t} = \frac{k_1[V]}{1+b_1[\mathrm{IFN}\beta]^{n_1}} - d_1[V] \tag{1}$$

$$\frac{\mathrm{d}[IRF7p]^{\mathrm{o}}}{\mathrm{d}t} = k_2[V]([IRF7_{\mathrm{total}}] - [IRF7p]^{\mathrm{o}}) - k_3^{\mathrm{o}}\frac{[\mathrm{ISG56}]^{n_2}}{1+b_2[\mathrm{ISG56}]^{n_2}}$$
$$+ k_4^{\mathrm{o}}[\mathrm{IFN}\beta] - d_2^{\mathrm{o}}[IRF7p]^{\mathrm{o}} \tag{2}$$

$$\frac{\mathrm{d}[\mathrm{IFN}\beta]}{\mathrm{d}t} = k_5^{\mathrm{o}}\frac{([IRF7p]^{\mathrm{o}})^{n_3}}{(b_3^{\mathrm{o}})^{n_3} + ([IRF7p]^{\mathrm{o}})^{n_3}} - d_3[\mathrm{IFN}\beta] \tag{3}$$

$$\frac{\mathrm{d}[\mathrm{ISG56}]}{\mathrm{d}t} = k_6[\mathrm{IFN}\beta] - d_4[\mathrm{ISG56}] \tag{4}$$

In Eq. (1), the replication of viral RNA is assumed to be linearly proportional to their concentrations based on the law of mass action. The negative feedback from IFNβ to viral RNA uses Hill equations. In Eq. (2), we assume that the sum of inactive IRF7 and phosphorylated IRF7 is a constant. The inactivated IRF7 is phosphorylated by the viral RNA, and the activation by IFNβ follows the law of mass action (the first and third terms). The negative feedback of ISG56 is described using the Hill function (the second term). In Eq. (3), the positive feedback of IRF7p is represented by the Hill function (the first term). The last term in all of the equations represents the degradation rate, following the law of mass action.

To make the analysis more convenient, we nondimensionalized the model by normalizing the total amount of IRF7 and made the following substitutions.

$$[IRF7p] = [IRF7p]^{\mathrm{o}}/[IRF7_{\mathrm{total}}], \quad k_3 = k_3^{\mathrm{o}}/[IRF7_{\mathrm{total}}] \tag{5}$$

$$k_4 = k_4^{\mathrm{o}}/[IRF7_{\mathrm{total}}], \quad b_3 = b_3^{\mathrm{o}}/[IRF7_{\mathrm{total}}] \tag{6}$$

where the parameters k_3^{o}, k_4^{o}, b_3^{o} and variable $[IRF7p]^{\mathrm{o}}$ correspond to the initial model. All of the simulations are based on the following non-dimensional equations.

$$\frac{d[V]}{\mathrm{d}t} = \frac{k_1[V]}{1 + b_1[\mathrm{IFN}\beta]^{n_1}} - d_1[V] \tag{7}$$

$$\frac{\mathrm{d}[IRF7p]}{\mathrm{d}t} = k_2[V](1 - [IRF7p]) - k_3\frac{[\mathrm{ISG56}]^{n_2}}{1 + b_2[\mathrm{ISG56}]^{n_2}}$$
$$+ k_4[\mathrm{IFN}\beta] - d_2[IRF7p] \tag{8}$$

$$\frac{\mathrm{d}[\mathrm{IFN}\beta]}{\mathrm{d}t} = k_5\frac{[IRF7p]^{n_3}}{{b_3}^{n_3} + [IRF7p]^{n_3}} - d_3[\mathrm{IFN}\beta] \tag{9}$$

$$\frac{\mathrm{d}[\mathrm{ISG56}]}{\mathrm{d}t} = k_6[\mathrm{IFN}\beta] - d_4[\mathrm{ISG56}] \tag{10}$$

The model includes 4 variables and 13 parameters. Some of the dimensionless parameters are set similar to the values reported in our previous work [18–20], and the other parameters are obtained through optimization of the difference between the simulation of the mathematical model and biological experimental data by the hybrid genetic algorithm proposed in [19]. The time series experimental dataset we used is that using vesicular stomatitis virus-infected MEFs

Table 1
The definitions and values of all parameters in ODE model.

Processes	Parameters	Values	Reference
Virus replication	k_1	0.088 h^{-1}	[20]
IRF7 induction	k_2	0.1482 h^{-1}	Estimated
ISG56 inhibit activation of IRF7	k_3	4.663 h^{-1}	Estimated
IRF7 induction	k_4	0.52 h^{-1}	[19]
IFNβ induction	k_5	0.8774 h^{-1}	[20]
ISG56 induction	k_6	0.205 h^{-1}	[19]
Virus degradation	d_1	0.0686 h^{-1}	Estimated
IRF7 degradation	d_2	0.62 h^{-1}	[19]
IFNβ degradation	d_3	0.1897 h^{-1}	[19]
ISG56 degradation	d_4	0.738 h^{-1}	Estimated
associate constant	b_1	2.798	Estimated
associate constant	b_2	3.17	Estimated
activation constant	b_3	0.782	Estimated
Hill coefficient	n_1	3	[19,36]
Hill coefficient	n_2	2	[19]
Hill coefficient	n_3	2	[19]

Table 2
The propensity functions related to the kinetic reactions and the number of molecules in the system is controlled by the system size Ω.

No	Reaction	Propensity function
1	Virus	$k_1\mathrm{Virus}/(1+b_1\mathrm{IFN}-\beta^{n_1}/(\Omega^{n_1}))$
2	Virus	$d_1\mathrm{Virus}$
3	IRF7p	$k_2\mathrm{Virus}(1-(IRF7p/\Omega))-k_3\Omega\mathrm{ISG56}^{n_2}/(\Omega^{n_2}+b_2\,\mathrm{ISG56}^{n_2})+k_4\mathrm{IFN}\beta$
4	IRF7p	$d_2\mathrm{IRF7p}$
5	IFNβ	$k_5\Omega IRF7p^{n_3}/((b_3\Omega)^{n_3}+IRF7p^{n_3})$
6	IFNβ	$d_3\mathrm{IFN}\beta$
7	ISG56	$k_6\mathrm{IFN}\beta$
8	ISG56	$d_4\mathrm{ISG56}$

obtained from our previous work [20]. The parameters obtained are shown in Table 1.

To show the reasonability of the proposed mathematical model, we simulate two types of experimental data obtained from [31]. One is the time series of Western Blot data for ISG56 and another is the inhibitory effects of ISG56 on the dynamics of virus-induced IFNβ signaling. Fig. 3 demonstrates that the simulation results are consistent with the experimental data. Therefore, the presented model could reflect the main characteristics of the virus-induced innate immune system we considered.

### 2.3. The Master equations and simulations

We supposed that the state of the system is $X(t_0) = x_0$, and defined the conditional probability density function $P(x, t|x_0, t_0)$, which is the probability of the system state satisfying $X(t) = x$ at time t.

The master equation was built according to the following probability equation:

$$\frac{\partial}{\partial t}P(x, t|x_0, t_0)$$
$$= \sum_{j=1}^{8} a_j(x - v_j)P(x - v_j, t|x_0, t_0) - a_j(x)P(x, t|x_0, t_0)] \tag{11}$$

where a_j is the propensity function corresponding to the chemical reaction channel j, and v_j is the state-change vector when reaction j occurred.

Following the modeling approaches for stochastic models [37], all of the propensity functions related to the 8 reactions in the ODE model are listed in Table 2, and parameters were set to be the same as those in Table 1. The stochastic simulations were performed using the Gillespie algorithm [38]. C. Rao et al. [39] have shown that quasi-steady state approximations (QSSA) remain valid in the stochastic case, but recent work [40–43] has shown that the stochastic QSSA for the Michaelis– Menten reaction is valid only in a subset of the
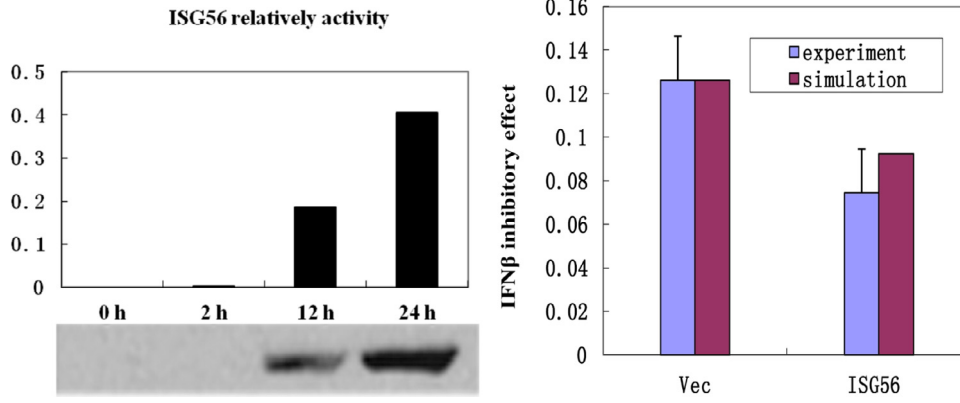
Fig. 3. (Color online.) Comparison between the numerical simulation and experimental results [31]. The left subfigure is the simulation results of ISG56 activity, and the figure below is the Western blot array; the right subfigure shows the inhibitory effects of ISG56 on the IFNβ.

biological parameter space and Hill exponents larger than one. In our simulation, the trend of stochastic simulation was the same as that of the deterministic equation when the system size Ω is set to 1000.

2.4. The Langevin equations and simulations

The Langevin equations were built as follows.

$$[V](t + dt) = [V](t) + \frac{k_1[V]}{1+b_1[IFN\beta]^{n_1}} - d_1[V]$$
$$+ \sqrt{\frac{k_1[V]}{1+b_1[IFN\beta]^{n_1}}} \zeta_1(t)(dt)^{1/2} \quad (12)$$
$$- \sqrt{d_1[V]}\zeta_2(t)(dt)^{1/2}$$

$$[IRF7p](t + dt) = [IRF7p](t) + k_2[V](1 - [IRF7p])$$
$$- k_3 \frac{[ISG56]^{n_2}}{1+b_2[ISG56]^{n_2}} + k_4[IFN\beta] \quad (13)$$

$$-d_2[IRF7p]$$
$$+ \left(\sqrt{k_2[V](1 - [IRF7p]) - k_3 \frac{[ISG56]^{n_2}}{1+b_2[ISG56]^{n_2}} + k_4[IFN\beta]}\right)$$
$$\times \zeta_3(t)(dt)^{1/2}$$
$$- \sqrt{d_2[IRF7p]}\zeta_4(t)(dt)^{1/2}$$

$$[IFN\beta](t + dt) = [IFN\beta](t) + k_5 \frac{[IRF7p]^{n_3}}{b_3^{n_3} + [IRF7p]^{n_3}} - d_3[IFN\beta]$$
$$\quad (14)$$
$$+ \sqrt{k_5 \frac{[IRF7p]^{n_3}}{b_3^{n_3} + [IRF7p]^{n_3}}} \zeta_5(t)(dt)^{1/2} - \sqrt{d_3[IFN\beta]}\zeta_6(t)(dt)^{1/2}$$

$$[ISG56](t + dt) = [ISG56](t) + k_6[IFN\beta] - d_4[ISG56]$$
$$+ \sqrt{k_6[IFN\beta]}\zeta_7(t)(dt)^{1/2} \quad (15)$$
$$- \sqrt{d_4[ISG56]}\zeta_8(t)(dt)^{1/2}$$

Where the $\zeta_i(t)$ is the Gaussian white noises with $\langle\zeta_i(t)\rangle = 0$ and $\langle\zeta_i(t)\zeta_j(t')\rangle = \delta_{ij}\delta(t - t')$, Ω is the system size. The simulation

of Langevin equations is performed using the Euler–Maruyama algorithm provided in [44].

2.5. The bifurcation analysis for a single parameter and two parameters

The single parameter bifurcation diagrams are computed by AUTO as incorporated in XPPAUT [45] and oscill8 [46].

We proposed a new method for calculating the bifurcation for two parameters in three dimensions. For a given system, we supposed that the system has impulsive dynamical behavior due to abrupt jumps at certain instances during the evolving process, and applied the bifurcation theory proposed in [47].

In the simulation, we captured the Poincaré cross section according to the phase diagram of the system and collected the last points of the corresponding variables at each considered repeated time interval by varying the bifurcation parameters at biologically reasonable intervals. The detailed pseudocode is shown as follows:

Initialize the variables of steady states(SS) for the system.
for the first parameter that varies in the biologically reasonable interval. **do**
　for the second parameter that varies in the biologically reasonable interval. **do**
　　Set the initial value for the variables.
　　Set the time span for the simulations Tspan=[0:step:n*period], step=0.1; period=2*pi.
　　the steady states of the system.
　　Set the obtained steady states as the initial value.
　　for i=1:m **do**
　　　Set the time span Tspan=[(i+n-1)*period:step:(i+n)* period];
　　　Obtain the steady state of the system and collect the steady states (SS) under the two corresponding parameters.
　　　Set the obtained steady states as the initial value.
　　end for
　end for
end for

To obtain relatively correct ultimate steady states in our simulation, we set the appropriate simulation period. The parameter n is set to 60, and the parameter m is set to 140. All of the other parameters are set to be the same as in the Table 1 in the simulations. The mesh bifurcation diagrams were obtained by plotting the parameter interval against the corresponding collect steady state of the system. The mesh bifurcation diagrams of two parameters in three dimensions captured the main dynamic feature of the system.

2.6. Stochastic simulations of the multi-cellular coupled model

During the simulations, each cell was simulated as an independent agent. The main components such as Virus, IRF7 and ISG56 in each cell accurately reacted to changes in its local environment affected by the diffusion of the IFN gene. Extracellular IFN was considered to be rapidly diffusing in cell culture and was iterated with the Euler method [48]. The parameters and propensity functions for a single cell were set to be the same as in the Tables 1 and 2, respectively. We assumed that all 1000 infected cells were in a well-mixed system with a fixed system size Ω, and all of the genes in the cells were inactive initially.

Assuming there are N cells, each cell corresponds to M different states, and each state has R reaction channels. The simulation procedure of a multi-state cell system using the Gillespie algorithm is shown as follows:

Algorithm 1 Gillespie algorithm for multi-cellular coupled model.

1. Initialize all cells in each state $X(N, R) = 0$, the cell state change variable $CS = 0$, the molecule state change vector V, and the virus initial amount; set the time $t = 0$.

2. Initially, assume that each cell starts from state one $X(N, 1)$, compute the propensity function for each cell$[A_1(x), A_2(x), \ldots, A_N(x)]$, $A_i = [a_{i1}(x), a_{i2}(x), \ldots, a_{iR}(x)]$ $(i = 1, \ldots, N)$,and add the reaction constants $a_0 = \sum_{i=1}^{N} \sum_{j=1}^{R} a_{ij}(x)$.

3. Generate a random number r_1 in $(0, 1)$, determine the time interval τ when the next reaction occurs by $\tau = (1/a_0)ln(1/r_1)$.

4. Generate a random number r_2 in $(0, 1)$, determine the occurred reaction channel i as well as the cell j using the following formulas: $b = reshape(X, 1, N * R)$, $\frac{1}{a_0}\sum_{k=1}^{s-1} b_k < r_2 < \frac{1}{a_0}\sum_{k=1}^{s} b_k$, $i = mod(s, R), j = [s/R]$.

5. Update the cell state change variable $CS(j) = CS(j) + CS(i)$, the number of molecules in the corresponding cell $X(j, i) = X(j, i) + V_{ji}$, the time $t = t + \tau$ and extracellular IFN.

6. Return to step 2 unless the simulation time has been exceeded or the number of reactants is zero.

---

3. Results

3.1. Bifurcation dynamics of positive and negative feedbacks

Feedback loops in signaling pathways play important roles in determining system dynamics. Thus, it is important to analyze the role

and impact of the positive and negative feedback loops emanating from virus-triggered innate immune signaling pathways.

The two subfigures of the bifurcation diagrams in Fig. 4 as a function of negative and positive feedback strengths showed that the bistable phenomenon exists when the positive feedback strength k_4 varies in the region [0.45, 1] and negative feedback strength k_3 falls in [4.663 10.663] (Fig. 4A). The system undergoes the transition from the monostability of a high level to a bistable switch and then to relaxation oscillation with an increase in the negative feedback strength. When the negative feedback strength k_3 is decreased to the threshold ($k_3 = 2.2$) or increased to the threshold ($k_3 > 10.663$), the bistable phenomenon disappears, and the expression of IFNβ remains at a high level. When the negative feedback strength is larger than approximately 10.663, the system exhibits oscillatory behavior (Fig. 4B). By increasing the strength of positive feedback strength k_4, the system undergoes a transition from monostability at a lower level to a bistable switch and then to monostability at a higher level. IFNβ exhibits a lower or higher level with steady states when the positive feedback strength is smaller than 0.45 or larger than 1.2, respectively.

The results shown that the system could switch from a high level to a low level by impairing the positive feedback strength only, while enhancement of the negative feedback can tune the system from bistability to oscillation. These findings reveal the possible biological mechanisms for irreversible bistability which will lead to over immunity (high state of IFNβ) or immunodeficiency (lower state of IFNβ) in the virus-triggered innate immune response [49,50].

As the stochastic fluctuations have been proven to exist in the induction of IFNβ in a real cell environment, stochastic switching between different states was considered. To compare the simulation results between the Master equation and Langevin equation, we randomly chose the initial value of the model in [0, 1], and performed stochastic simulations for the Master equation and Langevin equation using the Gillespie algorithm and Euler– Maruyama algorithm (See Models and Methods in 2.3 and 2.4), respectively.

We obtained the ultimate value as the steady state of the system through dividing the system size by the molecular numbers. Stochastic switching between the two stable steady states occurred (Fig. 5) for both stochastic equations. For the stochastic simulation results of the Langevin equation, the steady state is bound by a deterministic term (the upper steady state is lower than the deterministic term and the lower steady state is higher than the deterministic term). The distance between the two different states is smaller than normal under the Langevin equation. There is almost no bistability region of the stochastic simulation, and few cases corresponding to the mediate
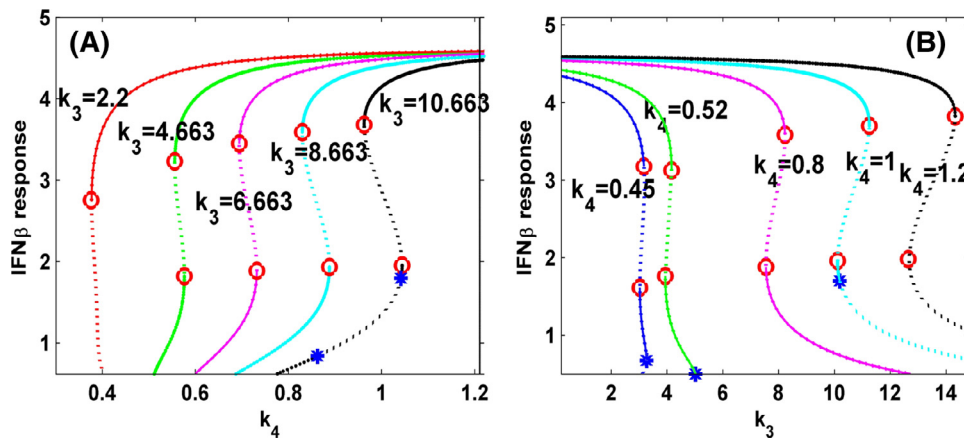
Fig. 4. (Color online.) The bifurcation diagrams of positive feedback strength (k_4) and negative feedback strength (k_3). (A) Bifurcation diagram of positive feedback strength (k_4) at different negative feedback strengths (k_3). (B) Bifurcation diagram of negative feedback strength (k_3) at different positive feedback strengths (k_4). Solid lines denote stable steady states, and dashed lines denote unstable steady states. The points corresponding to red circles and blue stars represent the Saddle nodes and Hopf bifurcation nodes, respectively. All of the other parameters are set to be the same as in Table 1.
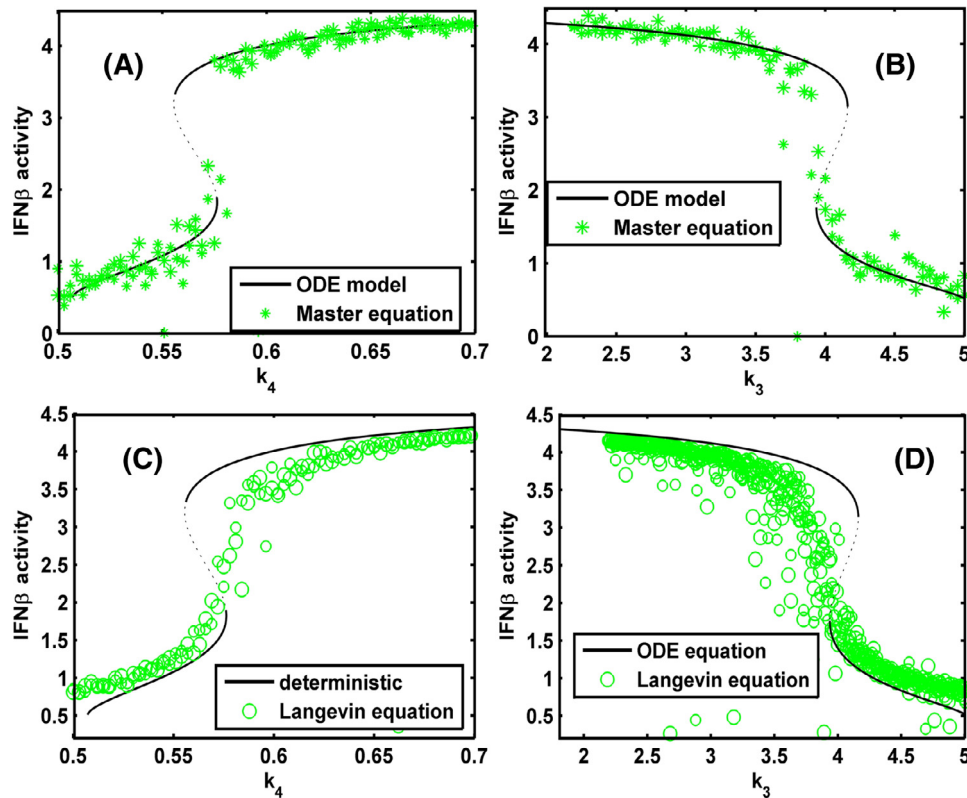
Fig. 5. (Color online.) The bifurcation diagrams of IFNβ concerning the positive feedback strength k_4 and negative feedback strength k_3 for comparison between the deterministic and the stochastic models. (A) and (B) compare the bistability of the ODE model with that of the Master equations for parameters k_4 and k_3, respectively; (C) and (D) compare the bistability of the ODE model with that of the Langevin equations for parameters k_4 and k_3, respectively. The black line corresponds to deterministic simulation, the green star and green circle correspond to the stochastic simulation results of the Master equation and Langevin equation, respectively. All of the other parameters are set to be the same as in Table 1.

state when the parameter k_3 and k_4 fell into the unsteady bistability range of the deterministic model. Although the steady state of zero has been neglected in the analysis of the deterministic case, it also exists in the stochastic case.

To compare the relative impact of the negative feedback strength k_3 and positive feedback strength k_4 on the expression of the IFNβ gene, two parameter bifurcations were analyzed and are shown in (Fig. 6A and B). The IFNβ displays a low or high steady state when the positive feedback strength varies in the range [0.3, 2]. The results show that the bistable phenomenon of IFNβ appears when k_3 and k_4 are set at a certain value. To characterize the dynamical features of the system more clearly, the bifurcation diagram of IFNβ for the ratio between k_3 and k_4 as well as k_4 was analyzed (Fig. 6C and D). Obviously, the Virus and IFNβ dramatically changed when varying the two parameters. The results show that the bistable phenomenon appears when the proportion of the k_3 and k_4 maintains a certain range.

To further depict the dynamics of the system, we made the bifurcations of IFNβ for the ratio between k_3 and k_4 under four different states of positive feedback strength k_4 as shown in Fig. A.15.

In the first state, when the positive strength k_4 is approximately 0.52, with an increase in the ratio of k_3 and k_4, the system undergoes a bistable switch from a high level to a low level and then exhibit oscillatory behavior; in the second state, when the positive feedback strength k_4 is approximately 0.95, the system runs into damped oscillation when the negative feedback strength is larger than the threshold. To exemplify this, we added the bifurcation diagram of k_3 using oscill8 software when the k_4 is set to 0.95 in the Appendix A (Fig. A.16). We can see that the system exhibits bistability between the two saddle nodes (SNs), and the system displays oscillation

between the two Hopf bifurcation nodes (HB). In the third state, when the positive feedback strength k_4 is approximately 1.05, the system displays relaxation oscillation when the negative feedback strength is larger than the threshold; in the fourth state, when the positive feedback strength k_4 is approximately 1.5, the system undergoes a transition from monostability of a high level to oscillation and then toward monostability of a high level with an increase of k_3. The detailed explanations of negative feedback modulating the amplitude and frequency of the oscillations are listed in the Appendix B, and the numerical result is presented in Fig. B.17.

The bifurcation analysis results show that the IFNβ could switch between two different steady states when the positive feedback is relatively small. If the positive feedback strength is sufficiently large, for example, when k_4 is larger than 1.5 the IFNβ exhibits oscillatory behavior in a small range and maintains a high steady state independent of the negative strength k_3. Under this condition, the system may run into an over immunity state, and the infected tissue undergoes serious inflammatory and apoptosis.

The positive feedback of IFNβ induced by IRF7 in cellular antiviral defense is essential for the late phase of type I IFN induction, which produces a large amount of antiviral proteins to inhibit the replication of virus and eliminate it. However, the system cannot switch from the high state when the negative feedback is not sufficient to impair type I IFN induction, and the overproduction of type I IFNs will result in over immunity. Altogether, our results suggest that the system is tunable by balancing the strength of the positive feedback and negative feedback. Thus, a moderate ratio between the positive and negative feedback strengths is required to ensure a reliable switch between different IFN concentrations to regulate the immune response. These findings also agree with the theoretical results in previous
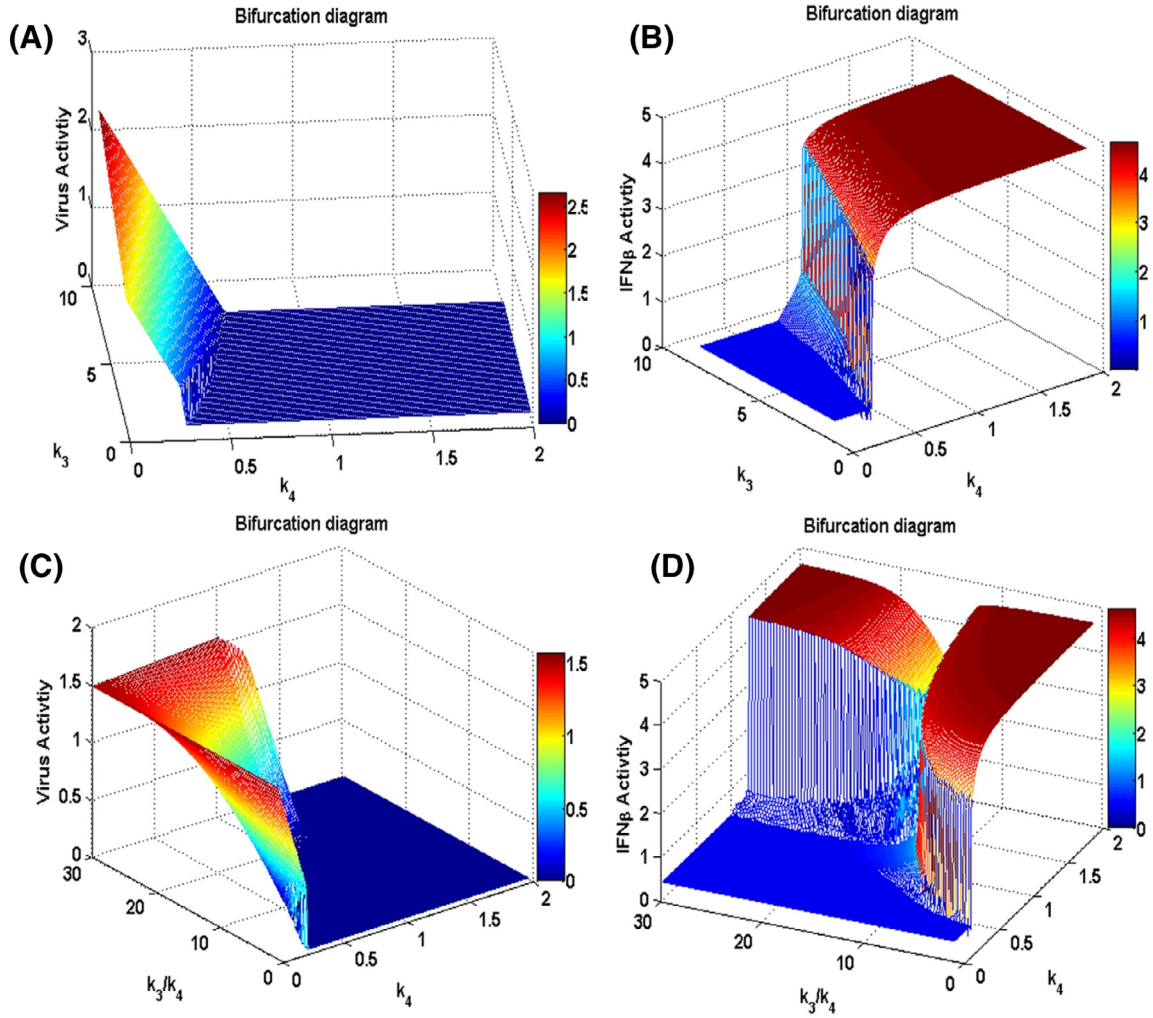
Fig. 6. (Color online.) The bifurcation diagrams of the steady states for Virus and IFNβ according to two parameters. (A, B) The bifurcation diagrams of negative feedback strength k_3 and positive feedback strength k_4 for Virus and IFNβ, respectively. (C, D) The bifurcation diagrams of positive feedback strength k_4 and the ratio between k_3 and k_4 for Virus and IFNβ, respectively. All of the other parameters are set to be the same as in Table 1.
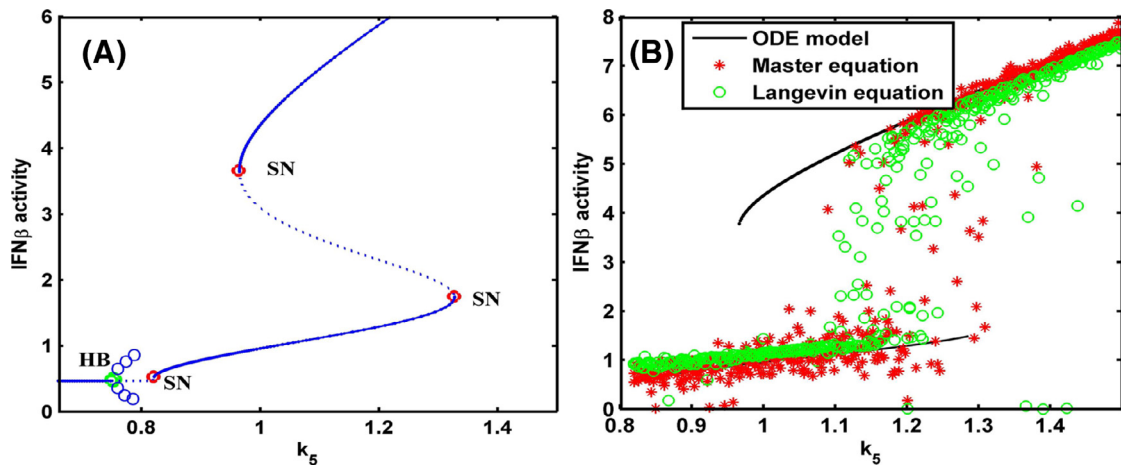
Fig. 7. (Color online.) The bifurcation diagrams of IFNβ as a function of k_5. (A) Thick and dashed blue lines correspond to stable and unstable steady states, respectively. The red and green circles denote saddle nodes (SNs) and Hopf bifurcation nodes (HBs), respectively. The open circles correspond to minima and maxima of the limit cycles. (B) The black line correspond to the simulation of the ODE equation, the red star and green circle are correspond to the stochastic simulation results of the Master equation and Langevin equation, respectively. All of the other parameters are set to be the same as in Table 1.
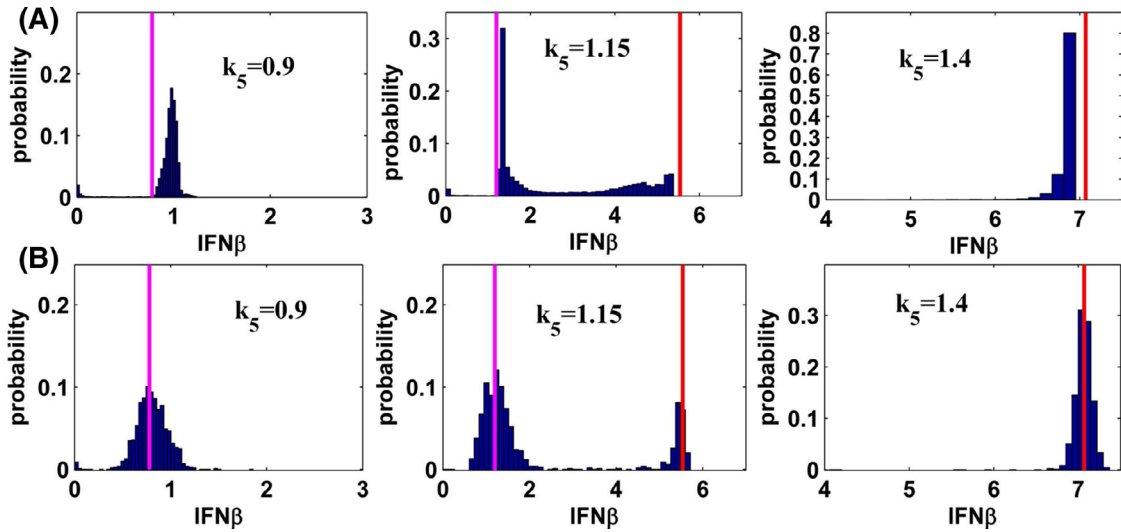
Fig. 8. (Color online.) The distribution diagrams of IFNβ under different values of k_5 for the Langevin and Master Equation. The distribution of IFNβ switching from the low to the high steady state by varying the parameters of k_5. (A) The subfigures are the simulation results from the Langevin equation. (B) The simulation results from the Master equation. The magenta line and red line correspond to the low and high steady states of the deterministic model, respectively. All of the other parameters are set to be the same as in Table 1.
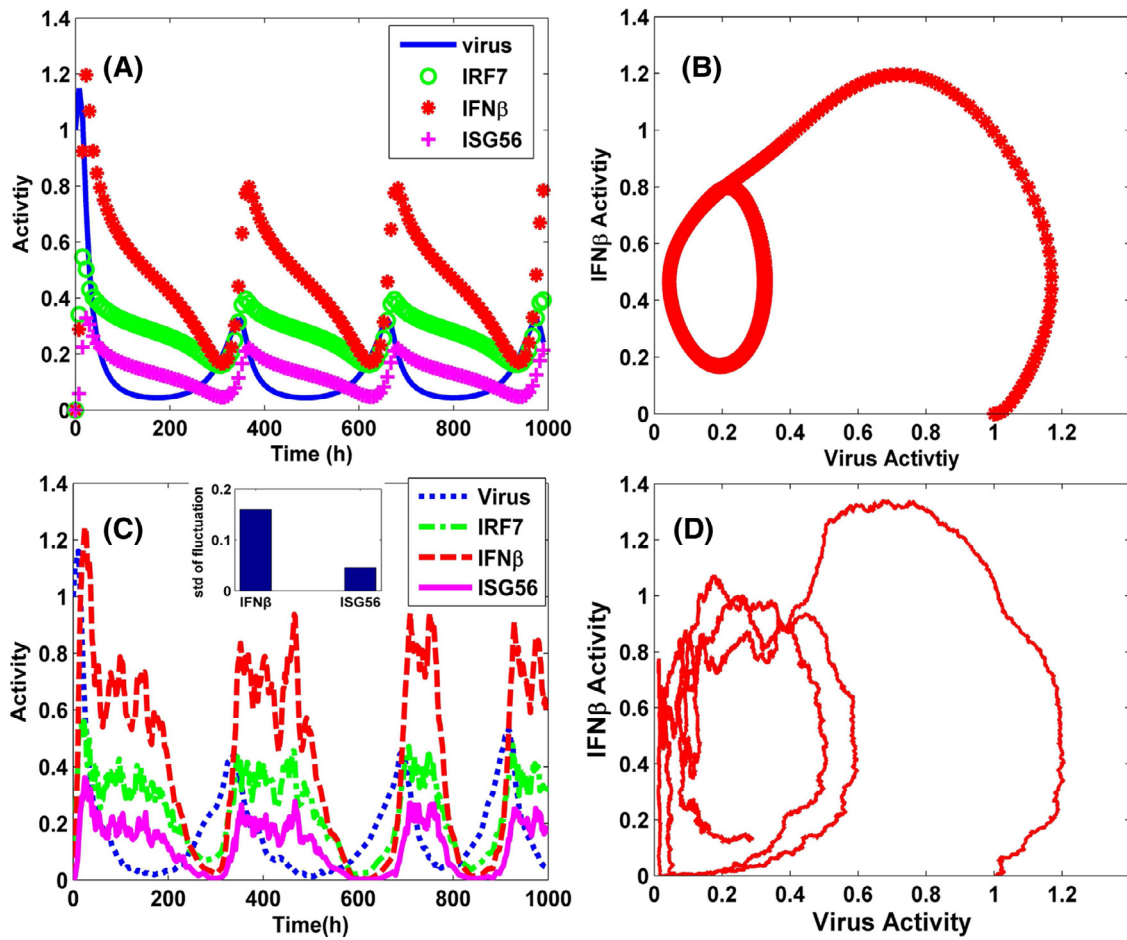
Fig. 9. (Color online.) The dynamic behavior of the system when the parameter k_5 is set to 0.77. (A) and (B) correspond to deterministic simulation. (C) and (D) correspond to stochastic simulation through the Gillespie algorithm. All of the other parameters are set to be the same as in Table 1.
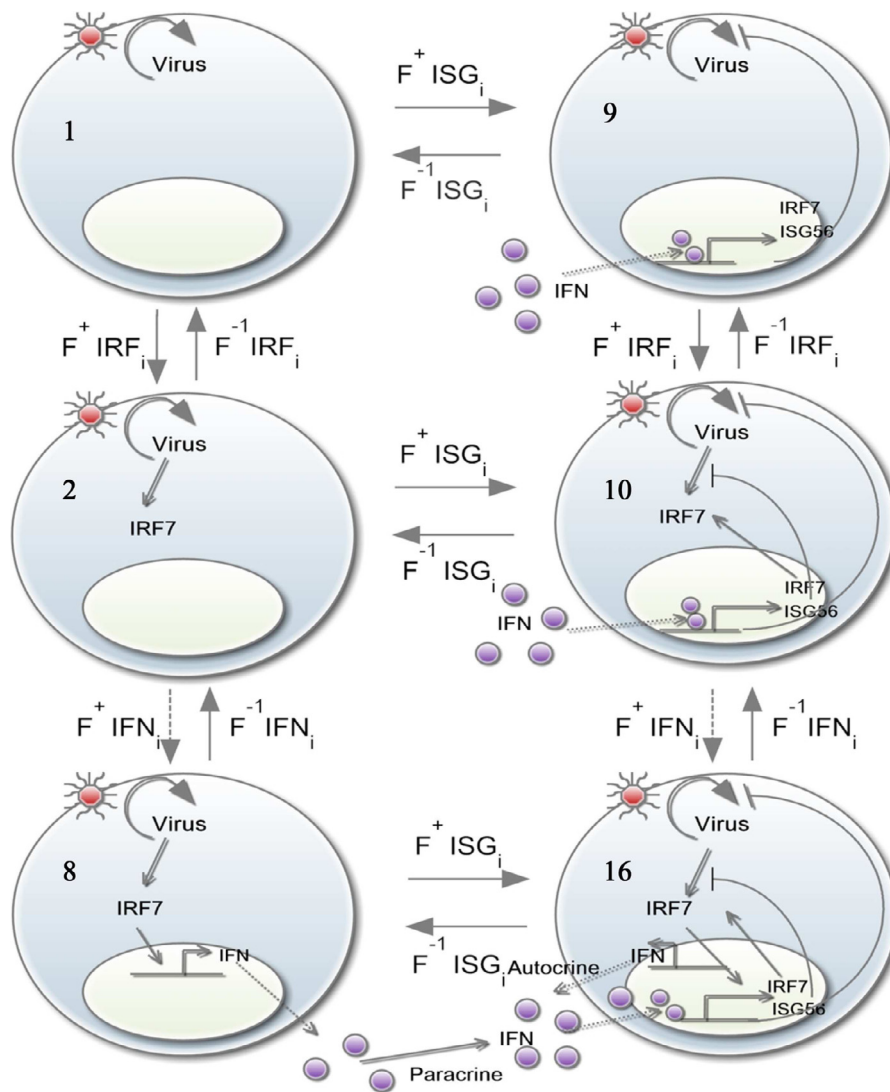
Fig. 10. (Color online.) The diagram of the state transitions of a single cell. The model of 16 states considered here describes a population of individual cells that contain the core transcriptional circuit coupled to double-negative feedback loops and a positive feedback loop involving four main components virus, IRF7, IFNs, ISG56, as well as cell communication via secreted IFN. The secreted IFNβ acts on the secreted cell itself or on a neighboring cell in an autocrine and paracrine manner [14].

studies [42,51]. Furthermore, the detailed description and analysis for the tenability of the dynamic behaviors between the two feedback strengths are presented in Appendix C.

### 3.2. The appropriate induction rate of IFNβ plays an important role in mediating the innate immune response

We explored the effects of IRF7 in the induction of IFNβ and the dependence of the steady state of IFNβ on its induction rate k_5. In the bifurcation of the diagram for the deterministic model (Fig. 7A), the steady state level of IFNβ can exhibit four distinct behaviors with an increase of k_5. For $0 < k_5 < 0.75$, there is a single low-level steady state. When $0.75 < k_5 < 0.82$, a limit cycle coexists with an unstable steady state. For $0.82 < k_5 < 0.95$, there exists one stable states. When $k_5 > 0.95$, bistability occurred.

To further investigate the bistable switch under the stochastic condition, we used two stochastic models to perform the stochastic simulations using the Gillespie algorithm and Euler–Maruyama algorithm when the parameter k_5 falls in the bistability range of the deterministic case [0.95, 1.33]. The simulation result (Fig. 7B) demonstrates that the system has a stochastic switch between two stable

steady states, and the steady state values do not change significantly when the intrinsic noise is characterized by the Master equation. However, the distance between the two stable steady states becomes smaller when simulating the Langevin equation.

Since noise plays an important role in the bistable system, we simulate the distribution of IFNβ in a collection of 10,000 cells under different values of k_5 for the Langevin equation and Master equation. Fig. 8 gives the distribution diagram of IFNβ switching from unimodal distribution of the low state ($k_5 = 0.9$) via the bimodal distribution in the bistable region ($k_5 = 1.15$) and then to the high state with unimodal distribution($k_5 = 1.4$) for the stochastic models by varying the parameter k_5. From the distribution histogram of IFNβ in the two stochastic models and deterministic model, we also statistically verified the conclusion that the distance between the two stable steady states in the Langevin model is smaller than that using the deterministic equation. Interestingly, the Master equation model maintains the stable steady states of the deterministic model.

The system exhibits oscillation when the induction rate of IFNβ k_5 is set to 0.77 (Fig. 9A and B), but the time series of IFNβ, ISG56 and IRF7 runs into nonstationary oscillation under the stochastic simulation (Fig. 9C and D).
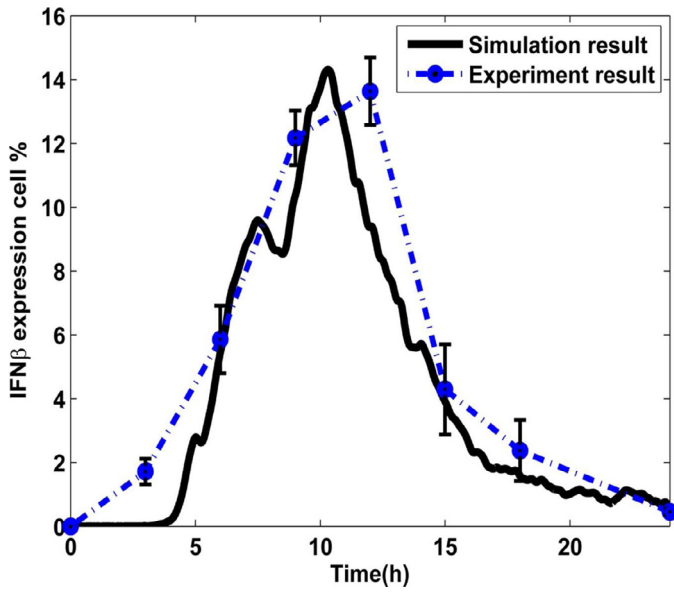
Fig. 11. (Color online.) Comparison between the simulation and experiment results of percentage of the IFNβ producing cells at different times after viral infection for the multi-cellular coupled system. The solid line is the simulation result, and the dotted line with the errorbar is the experimental result of Sendai virus infection of mouse MEF cell line originating from [9].

To measure the fluctuation of IFNβ and ISG56, we subtracted the deterministic simulation value from the corresponding stochastic simulation results and computed the standard deviation of the fluctuation values of IFNβ and ISG56, respectively. The result (subfigure in Fig. 9C) indicates that the noise in the innate immune system affects the expression of IFN more than the induction of ISG56, a finding that is supported by the recent experimental findings that the expression of IFN is stochastic, while the IFN-inducible antiviral genes are not stochastically expressed [9].

3.3. Stochastic simulation of the multi-cellular coupled system

In real organisms, the paracrine cell-to-cell communication is an efficient mechanism to protect host cells from viral infection. Ulfert Rand et al. [52] proposed a multi-cell mathematical model and revealed that a reliable antiviral response can be achieved through powerful paracrine propagation of the signal. Although the simulation results matched the experimental data of Newcastle Disease

virus-infected murine fibroblasts, they did not consider the negative feedback on the induction of IRF7 by ISG56; the propensity functions that they described were based on constants, and the virus induction of RIG and IFN were two independent parts. Therefore, it may not reflect the real protein fluctuations in the virus-triggered multi-cellular system.

In this study, we used the propensities defined in the deterministic equations and modeled the virus-triggered IFNβ induction in the multi-cellular system and iterated in parallel at the single-cell level. For each cell, the virus-triggered IFNβ gene induction was modeled as a multi-step process (Fig. 10), which is supported by the experimental observations in the published study [53]. A detailed description is presented in Appendix E.

The simulated percentage of IFN-expressing cells and comparison with experimental results are shown in Fig. 11. (The experimental data of Zhao et al. [9] exhibits the percentage of IFNβ expression in different mouse or human cells (L929 cells, MEF cells, RAW cells, primary foreskin fibroblast cells, MG63 cells and 293T cells) infected by the Sendai virus. Although the percentage of expressing cells differs between different cell lines, the trend is almost the same, and the maximal percentage did not exceed 20%). The simulation results qualitatively reproduced the experimental observations, indicating that the multi-state stochastic model we used is valid and effective.

3.4. The effects of the positive and negative feedback strength on the percentage of IFNβ expressing cells

Some experimental results showed that the cell-to-cell heterogeneity was a pervasive feature of the IFN system and can arise not only from the cell's intrinsic stochasticity occurring in the biochemical reactions but also from extrinsic factors such as differences in cell-cycle stage or cellular environment, which can be reflected in the kinetic parameters [54–56]. Here, we assumed that the intrinsic noise is determined by the fluctuations generated by the system size, and the extrinsic noise is defined as the fluctuations and variability in the kinetic parameters, particularly the positive feedback strength k_4 and negative feedback strength k_3 associated with the autocrine and paracrine of IFNβ.

To determine which mechanism is the main contributor of the IFNβ stochastic expression in the virus-triggered innate immune system, we simulated the multi-cellular coupled model by varying the system size Ω, the positive feedback strength k_4 and negative feedback k_3 (See Section 2.6 for the detailed method). The simulation results in Fig. 12 shows that the system size, negative feedback strength k_3 as well as positive feedback strength k_4 slightly affect the
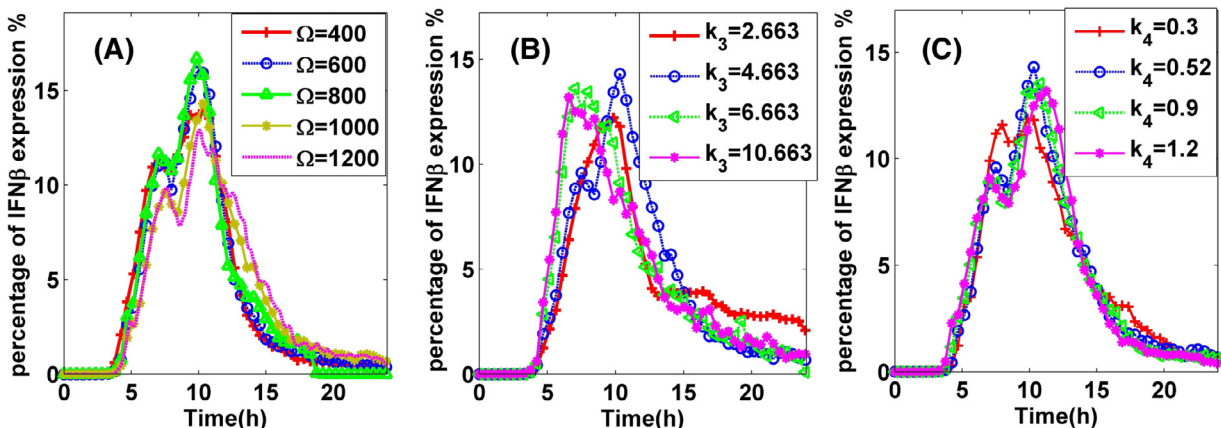
Fig. 12. (Color online.) Simulation results of the percentage of IFNβ expression and IFNβ activity under different Ω size (A), negative feedback strength k_3 (B) and positive feedback strength k_4 (C). All of the other parameters are set to be the same as in Table 1. For the subfigures B and C, the Ω is set to 1000.
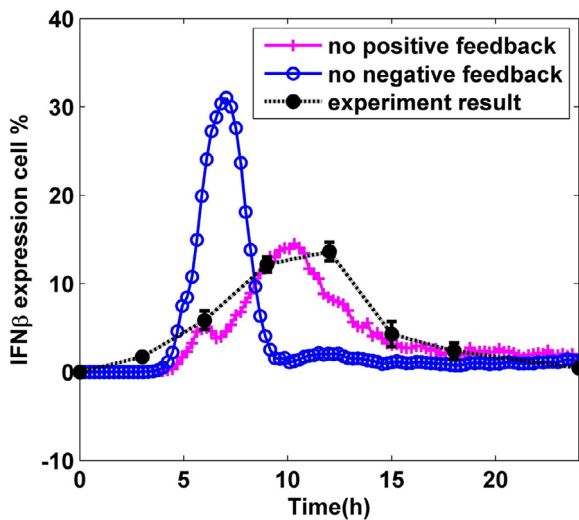
Fig. 13. (Color online.) Simulation results for the negative and positive feedback inhibition. The percentage of IFNβ-expressing cells without negative or positive feedback compared with the experimental data.

percentage of IFNβ expression, suggesting that these may not be the main sources of the stochastic expression mechanism.

3.5. Negative feedback inhibition greatly affects the percentage of IFNβ expressing cells

Furthermore, to investigate the mechanism of stochastic expression, we simulated the system under two extreme conditions in which the negative and positive feedbacks are inhibited, respectively. Simulation results (Fig. 13) show that, when the negative feedback inhibition is presented, the percentage of IFNβ expressing cells increased sharply with time, the maximum proportion is larger than that in the normal state, and the time point corresponding to the maximum percentage was shorter than that in the normal state. This result indicates that the negative feedback on the activation of IRF7 may be the main source of the stochastic expression of IFNβ, a finding that is supported by the experimental findings that the stochastic expression of the IFN gene is a consequence of cell-to-cell differences in limiting the cellular components required for IFN induction [8], and the majority of cells translocating IRF7 to the nucleus also activated the IFNβ promoter [9].

On the one hand, the negative feedback of ISG56 on the activation of IRF7 limits the percentage of IFNβ that virus-infected cells can produce. The secreted IFNβ acts on cells that infected but are not producing IFNβ in the paracrine system and triggers an antiviral immune response by the expression of IFN-stimulated genes (ISGs). The produced intermediate levels of IFNβ are sufficient to block viral propagation. On the other hand, the negative feedback buffers the sharp increase in IFNβ-expressing cells, contributing to the even distribution of IFNβ, and thus avoiding over-expression of IFNβ in infected cells.

4. Discussions

Previous studies have concentrated on the analysis of a deterministic model or stochastic model independently. In this study, we provided a quantitative link between earlier unobservable signaling dynamics and type I IFN responses by unifying the deterministic model with the multi-cellular coupled stochastic multi-state model. For the deterministic model, the positive feedback guarantees an essential gradient for the bistable switch and shapes the diverse dynamical behavior of IFNβ coordinately with negative feedback. However, for the multi-state stochastic model, the noise and positive feedback effect is

less in the stochastic expression pattern of IFNβ, while the negative feedback through ISG56 on the inhibition of activation of IRF7 mediates the stochastic expression of IFNβ as an efficient mechanism for the antiviral response.

Earlier research suggested that noise has great effects on the dynamic activity of the system [57,58]. In our study, the minor effects of noises on the system mainly refer to the characteristics of the system such as the bistable phenomenon of the rate equation exhibited.

Due to the complexity of interlinked regulatory networks underlying the virus- triggered innate immune response, we considered a simplified regulatory module in this study. The model captured the main properties of the innate immune system. However, more comprehensive model is needed to interpret the details of the mechanism of the innate immune response. For example, the IFN induced the Janus kinase/signal transducer and activator of transcription (JAK–STAT) signaling pathway involving some feedback mechanisms [10] should be incorporated into the mathematical model. In addition, the proposed multi-cell coupled multi-state stochastic model needs much computing power for stochastic simulation. It is important to develop a more efficient algorithm for simulating this model in a further study.

Another major issue in modeling study is the accuracy of mathematical models. The current trend in computational modeling of biochemical systems is to construct more and more mechanistically detailed and thus complex models. However, the complexity of biological networks and lack of experimental data have put a limitation on the complexity of mathematical models. In addition to the widely used Michaelis– Menten kinetics and Hill functions, a number of approaches have been designed to reduce the complexity of biochemical reaction networks [59–62]. However, the cost of such simplification may be the accuracy of developed model. Recent research has shown that the conclusion from a simplified model may be conditional to the assumption of the model [41,43]. A similar case is the development of stochastic model or multi-scale model based on the developed deterministic model [37,39] (including this research work). Recent works also show that additional conditions should be applied if we hope to get precise simulation results [40,42]. Thus more research work is strongly needed to investigate the functions of noise and genetic regulations under the proper and correct conditions. All these issues are potential topics of our future research.

5. Conclusions

In this study, we proposed two stochastic models (the chemical Master equation and Langevin equations), and analyzed and compared two classes of models—i.e., deterministic ordinary differential equations (ODEs) and stochastic models (Master and Langevin equations)—to elucidate the dynamics and stochasticity in type I IFN signaling pathways. The simulation results show that the stochastic system displays a stable bistable switch, and the distance between the two stable steady states becomes smaller for the Langevin equation characterized system.

In addition, the coupled feedback loops enable the antiviral systems to produce perfect responses to virus infection, and a sustained constant signal input stimulation that produces a bistable switch might designate a decision-making phase where the cell can integrate various other stimuli before committing to a biological decision. The results suggest that the coupled positive and negative feedback loops form essential signal transduction modules in cellular antiviral innate immune signaling systems, which coordinately shape the virus-triggered type I IFNs response and may offer diverse regulating options.

To reveal the mechanism of IFNβ stochastic expression in infected cells, we further constructed a stochastic multi-cellular model based on the core deterministic model. Through extensive stochastic simulation and analysis, we found that the perturbation of positive

feedback regulation, as well as negative feedback strength and system size has a less effect on the stochastic expression of IFNβ; however, the negative feedback of ISG56 on the inhibition of IRF7 phosphorylation mainly contributes to the stochastic expression pattern of IFNβ.

In summary, our work bridges an important gap between the deterministic model that captures the system dynamics and stochastic model that characterizes the single cell level. This study not only represents a major step toward the comprehensive understanding of the mechanism of innate immune response but also provides certain guidance for further biological experiments.

Acknowledgments

Appendix A. Parameter sensitivity analysis

To analyze how the system responds to perturbation of the parameters, we performed sensitivity analysis of the parameters. The Fig. A.14 profiles the sensitivity of the input parameter to all of the variables in the model under the perturbation of 10% using the PRCC method [63]. The calculated PRCC is a standardized sensitivity measurement between -1 and 1 such that a negative value indicates an inverse relationship between the parameter and output, and a positive value indicates a positive relationship. From the Fig. A.14, we can see that the k_4(IFNβ positive feedback strength) showed relatively significant effects on IFNβ expression, and the other parameters had a relative slight effect or almost no effect on IFNβ expression.

As the reaction we considered in this model follows the timescale separation, the parameters in the non-elementary reaction rate functions are robust under perturbation, and the sensitivity of the non-
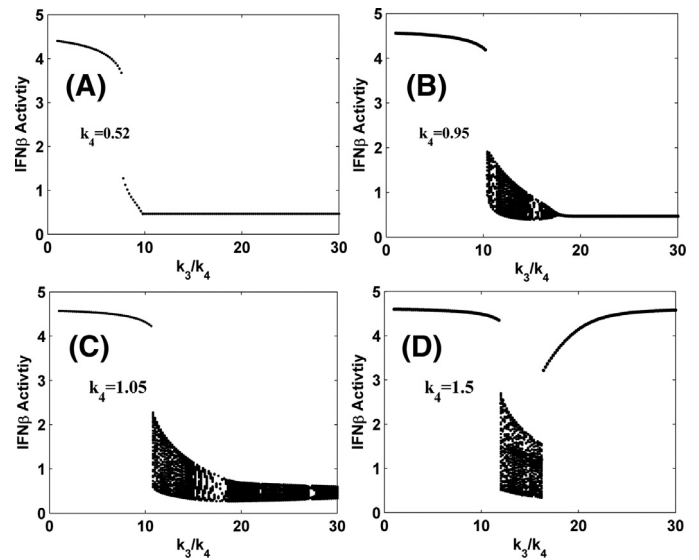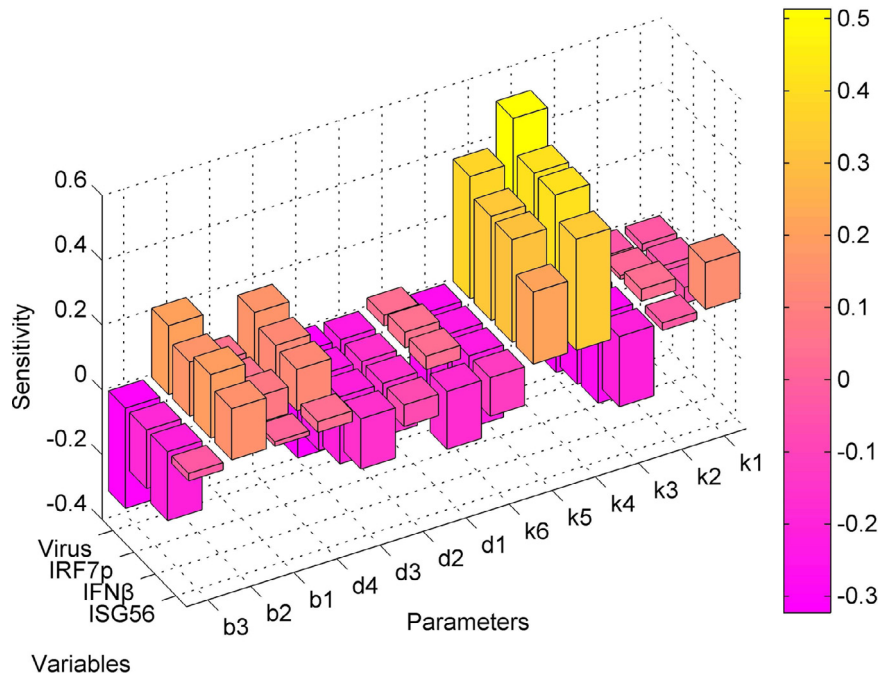

Fig. A15. (Color online.) The bifurcation diagram of IFNβ steady state when varying the ratio of k_3 and k_4 under four different positive feedback strength, while the positive feedback is increased from 0.52, 0.95, 1.05 and 1.5 corresponding to A, B, C and D, respectively. All of the other parameters are set to be the same as in Table 1.

elementary reaction rate functions in the model is small. Additionally, the reactant stationary assumption is satisfied. According to the recent progresses in the stochastic simulation reported in [40–43,64], the stochastic quasi-steady state approximation we obtained is accurate and valid under a certain subset of the biological parameter space.

Appendix B. Negative feedback regulate the amplitude and frequency of oscillation

To analyze the effects of the negative feedback strength on the oscillation of the system, we fixed the positive feedback strength

Fig. A14. (Color online.) The Sensitivity analysis to the perturbation of parameters in the model.
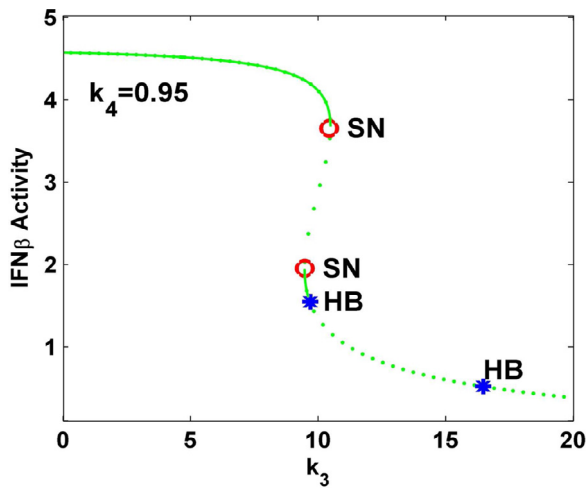
Fig. A16. (Color online.) The bifurcation diagram of k_3 with oscill8 software when the k_4 is set to 0.95. All of the other parameters are set to be the same as in Table 1. The red circle refers to the saddle node (SN), and the blue star refers to the Hopf bifurcation node (HB).

k_4 at 1 and varied the negative feedback strength k_3 at three different values: 10.663, 12.663 and 15.663. The simulation results showed that the system runs into oscillations (Fig. B.17). The oscillation amplitude is decreased when we further increased the negative feedback strength, while the period of the oscillation is increased. The results demonstrate that the negative feedback plays an important role in modulating the amplitude and frequency of the oscillations.

Appendix C. Tunability of the dynamic behaviors between the two parameters

As illustrated above, the negative and positive feedback coordinately contribute to the various dynamic behaviors. Fig. C.18 presents an overview of the turnability using the phase diagram of the IFNβ dynamics in the $k_3 - k_4$ spanned space. The diagram is composed of three types of dynamics: monostability, bistability and oscillation. Because the negative feedback was depicted by a hill function

term, we further analyzed the effect of the coefficient of the negative feedback b_2 on the system dynamics. By increasing the coefficient of the negative feedback b_2, the bistable and oscillate areas are decreased.

Obviously, we can see that the values of the negative and positive feedback strength can be cooperatively tuned in the corresponding regions to achieve desirable behaviors and functions. Similarly, the bifurcation diagram in the space spanned by k_4 and k_5 (Fig. C.19A) as well as the bifurcation diagram in the space spanned by k_5 and k_6 (Fig. C.19B) was analyzed, and the three types of dynamics of the system also exist.

Appendix D. Constant signal input drive diverse response when tuning the positive feedback and negative feedback strength

Switch-like behavior was found across a wide range of biological systems [65–67]. Positive feedback is a common mechanism enabling biological systems to respond to stimuli in a switch-like manner, and it has been demonstrated that the system robustly increases its responsiveness while precisely tuning the response to a consistent level in the presence of varying stimuli [68].

To explore the detailed mechanism of the system, we assumed that the system is stimulated by a constant signal and evaluated the steady state as well as the response time of the system; the response time was defined in the Methods section. We changed the strength of the feedbacks to explore its effects on switch while keeping the other parameters fixed. The input signal was denoted by S, and we plotted the response as a function of log(S). Simulation results (Fig. D.20A and C) showed that the system exhibited a switch-like response when we increased the positive feedback strength and negative feedback strength, but the trend of the steady states with input signal was opposite. (Fig. D.20A) With an increase in the positive feedback strength k_4, the steady state switched from a low state to a moderately high state. When k_4 is larger than 0.5, the steady state of the system increases to a higher steady state. However, the steady state of the system decreased with an increase in the signal input, and ultimately reached the moderate steady state. (Fig. D.20C) The system exhibits an opposite switch pattern with an increase in negative feedback strength k_3. When k_3 is smaller than 4, the system undergoes the transition from a much higher state to a moderate high state. However, when k_3 is approximately larger than 4, the system undergoes the transition from a low state to a higher state. In the first case, the
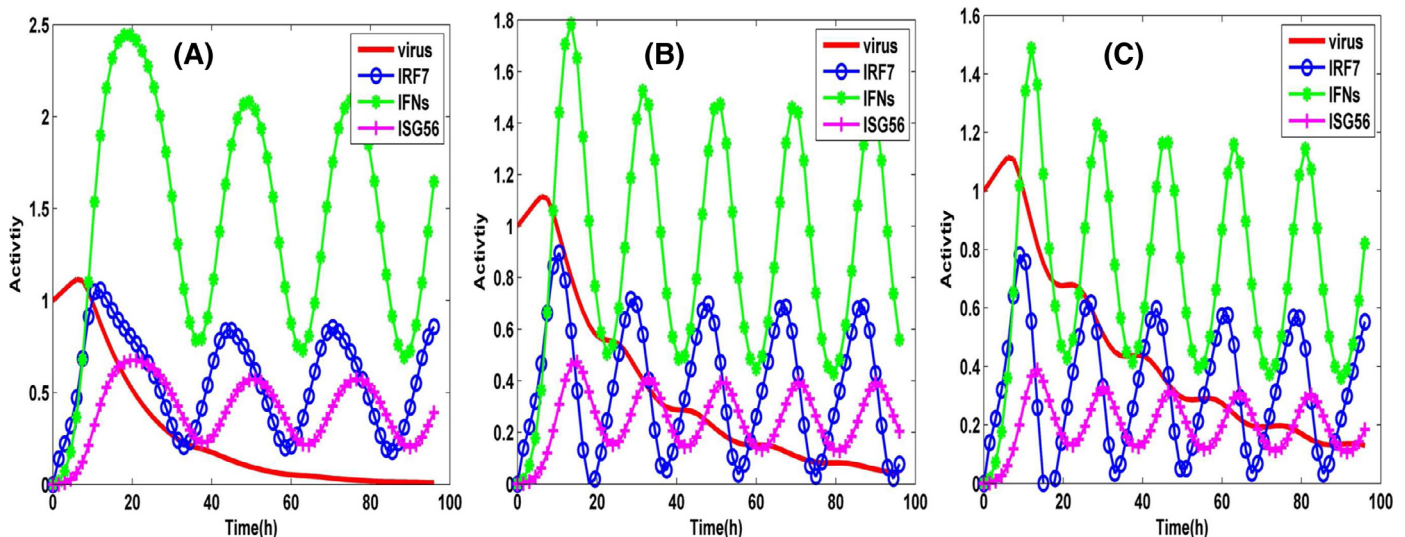
Fig. B17. (Color online.) The dynamic behavior of the system when the negative feedback strength k_3 is increased from 10.663 to 12.663 and 14.663, while the positive feedback strength k_4 is fixed at 1. All of the other parameters are set to be the same as in Table 1.
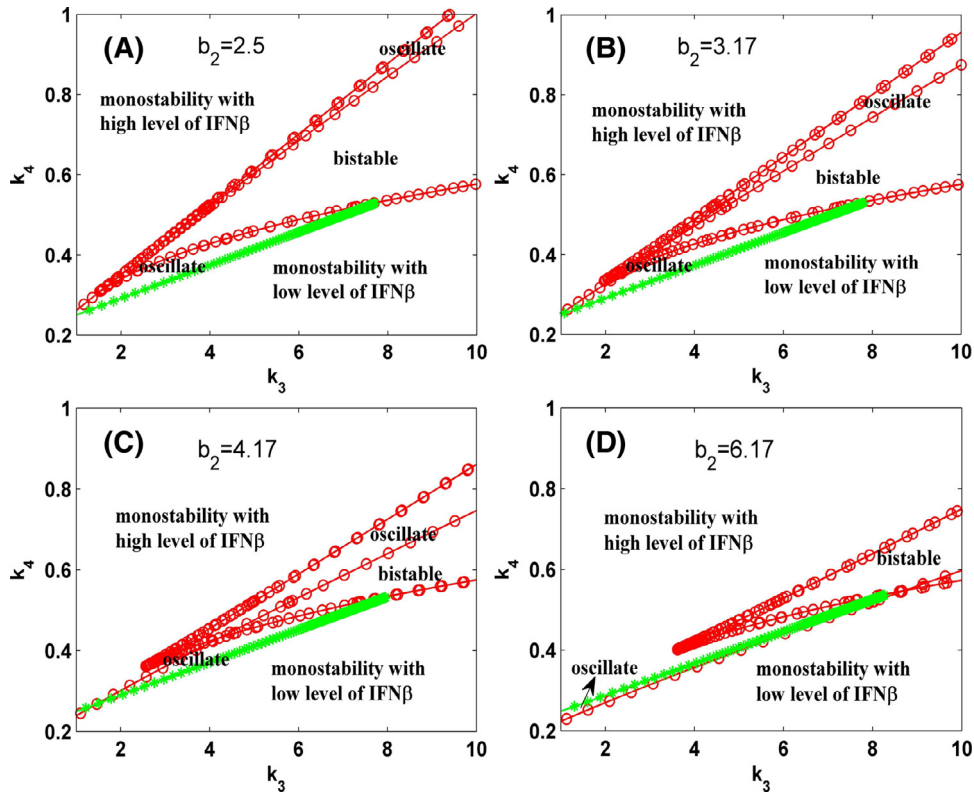
Fig. C18. (Color online.) Bifurcation diagram in the space spanned by the positive feedback strength (k_4) and negative feedback strength (k_3). With b_2 varying in [2.5, 6.17], the subfigures A, B, C and D correspond to $b_2 = 2.5$, $b_2 = 3.17$, $b_2 = 4.17$ and $b_2 = 6.17$, respectively. The diagram of the dynamical behavior of the system is composed of four regions: monostability with a high state and low state, bistability and oscillation. All of the other parameters are set to be the same as in Table 1.
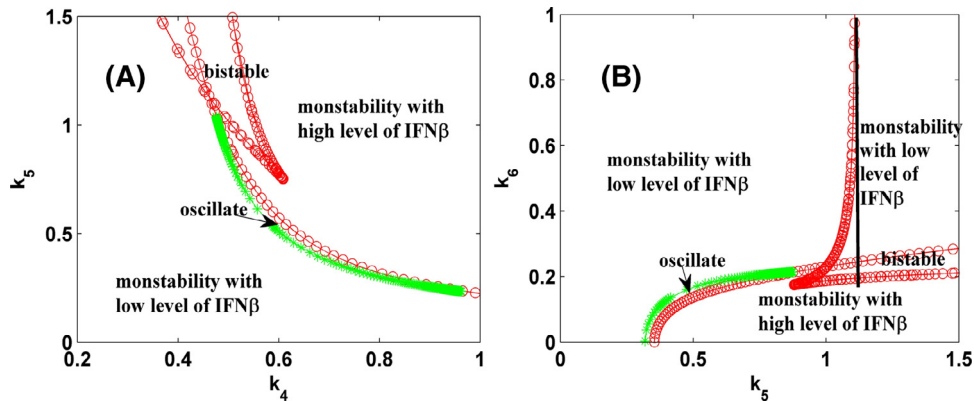
Fig. C19. (Color online.) (A) Bifurcation diagram in the space spanned by the positive feedback strength (k_4) and IFNβ induction rate (k_5). (B) Bifurcation diagram in the space spanned by the IFNβ induction rate (k_5) and ISG56 induction rate (k_6). The red circles and green stars on the borderlines denote the saddle-node and Hopf bifurcations, respectively. All of the other parameters are set to be the same as in Table 1.

upper threshold changes moderately; in the second case, the lower threshold changes moderately, while the ultimate state of the two cases is the same.

The response time (Fig. D.20B and D) is decreased with an increase in positive feedback strength or negative feedback strength when the added signal is large enough the response time coverage to a single line, indicating that, under conditions of transient stimulation, the system ultimately coverage the same state. (Fig. D.20E and F) The steady state and response time correspond to three different states: normal, system without positive feedback and system without negative feedback. The three different initial levels correspond to different states, but the different initial levels converge to the same level with an increase in the input signal strength.

The positive feedback and negative feedback cooperate to shape the switch response of the system, indicating that the appropriate combination of positive feedback and negative feedback can improve the ability of the bistable switches in the system.

Appendix E. Description of 16 states in multi-step process

(1) Fig. 10 presented 6 states (states 1, 2, 8, 9, 10 and 16).
(2) The transition between state 2 and state 8 describes the nuclear translocation of the key transcription factor IRF7. This process also contains 6 steps that correspond to states 3–8, respectively.
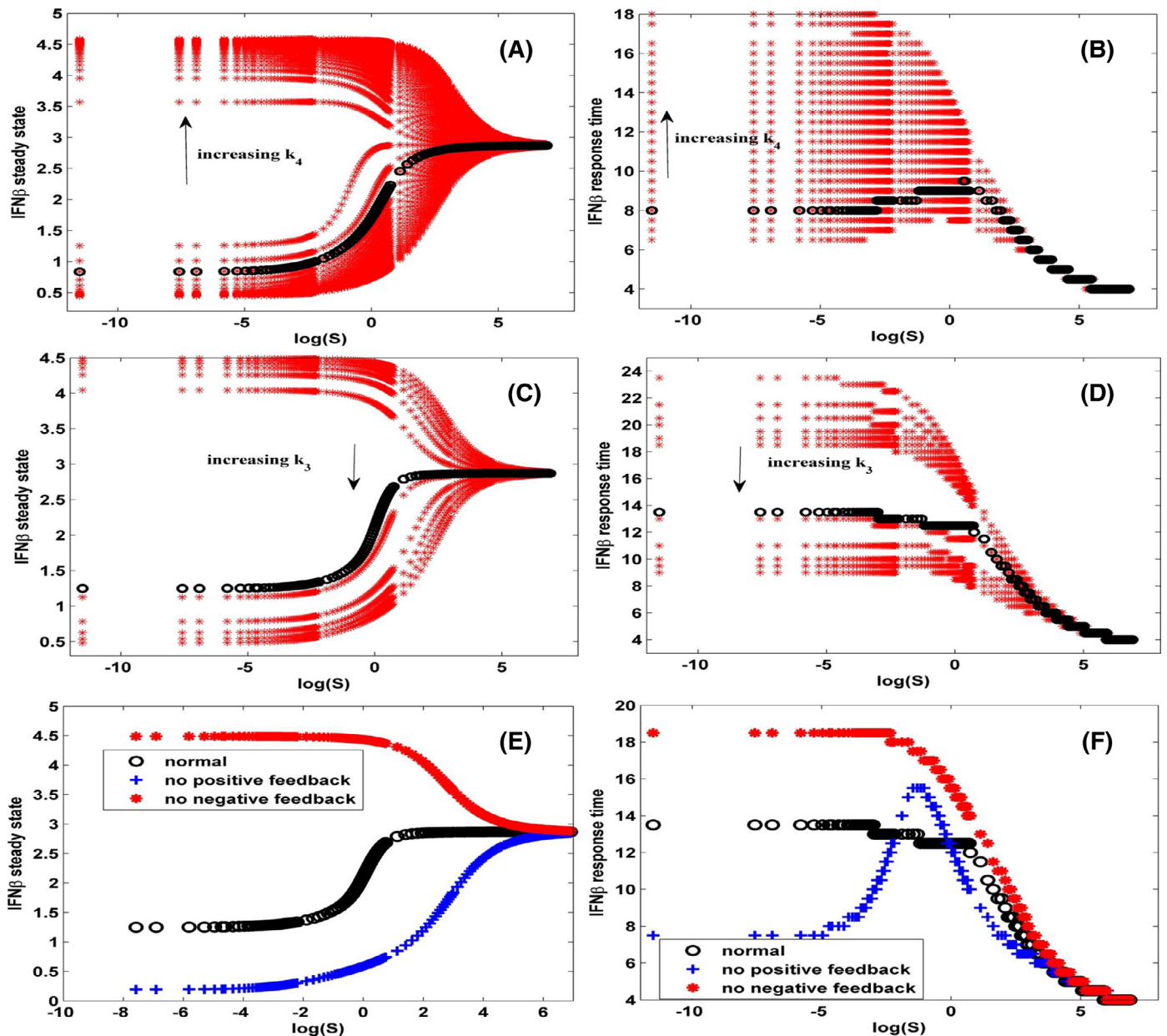
Fig. D20. (Color online.) The signal-response curves of the system. (A, B) The strength of positive feedback increases from 0.1 to 1.5 at a 0.1 step. (C, D) The strength of the negative feedback increases from 0 to 8 at a 0.8 step; the other parameters are set as Table 1. (A, C) correspond to the steady state of the system and (C, D) are corresponding to the response time when increasing the positive feedback and negative feedback strength. (E and F) The signal– response curve under three different states: normal, system without positive feedback and system without negative feedback. Note that the line with the black circle corresponds to default parameters as in Table 1, the red star denotes the case when there is no negative feedback, and the blue plus corresponds to no positive feedback case. All of the other parameters are set to be the same as in Table 1.

(3) The transition between state 10 and state 16 describes the process of the activation of IFN mRNA induction. This process also contains 6 steps that correspond to states 11–16, respectively. Therefore, there are a total of 16 different states in the multi-step process.

References

[1] R. Medzhitov, Recognition of microorganisms and activation of the immune response, Nat. 449 (2007) 819–826.
[2] C. Basset, J. Holton, R. O'Mahony, I. Roitt, Innate immunity and pathogen-host interaction, Vaccine 21 (Suppl 2) (2003) S12–23.
[3] T. Ganz, Defensins: antimicrobial peptides of innate immunity, Nat. Rev. Immunol. 3 (2003) 710–720.
[4] S.T. Li, L.Y. Wang, M. Berman, Y.Y. Kong, M.E. Dorf, Mapping a dynamic innate immunity protein interaction network regulating Type I interferon production, Immunity 35 (2011) 426–440, doi:10.1016/j.immuni.2011.06.014.
[5] H.C. McCanna, H. Nahalb, S. Thakura, D.S. Guttmana, Identification of innate immunity elicitors using molecular signatures of natural selection, PNAS 109 (2012) 4215–4220, doi:10.1073/pnas.1113893109.
[6] R. Zawatzky, E. De Maeyer, J. De Maeyer-Guignard, Identification of individual interferon-producing cells by in situ hybridization, Proc. Natl. Acad Sci. USA 82 (1985) 1136–1140.
[7] J. Hu, S.C. Sealfon, F. Hayot, C. Jayaprakash, M. Kumar, A.C. Pendleton, A. Ganee, A. Fernandez-Sesma, T.M. Moran, J.G. Wetmur, Chromosome-specific and noisy IFNB1 transcription in individual virus-infected human primary dendritic cells, Nucleic Acids Res. 35 (2007) 5232–5241.
[8] J.Z. Hu, G. Nudelman, Y.S. Shimoni, M. Kumar, Y.M. Ding, C. López, F. Hayot, J.G. Wetmur, S.C. Sealfon, Role of cell-to-cell variability in activating a positive feedback antiviral response in human dendritic cells, PLoS One 6 (2011) e16614.
[9] M.W. Zhao, J.W. Zhang, H. Phatnani, S. Scheu, T. Maniatis, Stochastic expression of the interferon β gene, PLoS Biol. 10 (2012) e1001249.
[10] T. Maiwald, A. Schneider, H. Busch, S. Sahle, N. Gretz, T.S. Weiss, U. Kummer, U. Klingmuller, Combining theoretical analysis and experimental data generation reveals IRF9 as a crucial factor for accelerating interferon alpha-induced early antiviral signalling, FEBS J. 277 (2010) 4741–4754, doi:10.1111/j.1742-4658.2010.07880.x.

[11] S. Jin, Y. Li, R. Pan, X. Zou, Characterizing and controlling the inflammatory network during influenza a virus infection, Scientific Rep. 4 (2014) 3799, doi:10.1038/srep03799.

[12] Y. Wang, J. Tan, F. Sadre-Marandi, J. Liu, X. Zou, Mathematica, modeling for intracellular transport and binding of HIV-1 gag proteins. Math. Bio. 261 (2015) 198–205, doi:10.1016/j.mbs.2015.01.008.

[13] J. Tan, X. Zou, Optimal control strategy for abnormal innate immune response, Comput. Math. Meth. Med. 2015 (2015) 386235, doi:10.1155/2015/386235.

[14] S. Hwang, K. Hur, J. Kim, K. Cho, S. Kim, J. Yoo, Biphasic RLR-IFN-β response controls the balance between antiviral immunity and cell damage, J. Immunol. 190 (3) (2013) 1192–1200, doi:10.4049/jimmunol.1202326.

[15] D. Levin, D. Harari, G. Schreiber, Stochastic receptor expression determines cell fate upon interferon treatment, Mol. Cell. Biol. 31 (2011) 3252–3266, doi:10.1128/MCB.05251-11.

[16] M.S. Suthar, M.M. Brassil, G. Blahnik, A. McMillan, H.J. Ramos, S.C. Proll, S.E. Belisle, M.G. Katze, M. Gale Jr., A systems biology approach reveals that tissue tropism to west nile virus is regulated by antiviral genes and innate immune cellular processes, PLoS Pathog. 9 (2) (2013) e1003168, doi:10.1371/journal.ppat.1003168.

[17] Y. Li, S. Jin, L. Lei, Z. Pan, X. Zou, Deciphering deterioration mechanisms of complex diseases based on the construction of dynamic networks and systems analysis, Scientific Rep. 5 (2015) 9283, doi:10.1038/srep09283.

[18] J. Tan, X. Zou, Complex dynamical analysis of a coupled system from innate immune responses, Int. J. Bifurcation and Chaos 23 (11) (2013) 1350180.

[19] W. Zhang, X. Zou, Systematic analysis of the mechanisms of virus-triggered type I IFN signaling pathways through mathematical modeling, IEEE/ACM Trans. Comput. Biol. Bioinform. 10 (2013) 771–779, doi:10.1109/TCBB.2013.31.

[20] J. Tan, R. Pan, L. Qiao, X. Zou, Z. Pan, Modeling and dynamical analysis of virus-triggered innate immune signaling pathways, PLoS One 7 (2012) e48114, doi:10.1371/journal.pone.0048114.

[21] J. Andrejeva, K.S. Childs, D.F. Young, T.S. Carlos, N. Stock, S. Goodbourn, R.E. Randall, The V proteins of paramyxoviruses bind the IFN-inducible RNA helicase, mda-5, and inhibit its activation of the ifn-beta promoter, Proc. Natl. Acad. Sci. USA 101 (2004) 17264–17269.

[22] M. Yoneyama, M. Kikuchi, T. Natsukawa, N. Shinobu, T. Imaizumi, M. Miyagishi, K. Taira, S. Akira, T. Fujita, The RNA helicase RIG-I has an essential function in doublestranded RNA-induced innate antiviral responses, Nat. Immunol. 5 (2004) 730–737.

[23] K. Honda, T. Taniguchi, IRFs: master regulators of signaling by toll-like receptors and cytosolic pattern-recognition receptors, Nat. Rev. Immunol. 6 (2006) 644–658.

[24] M. Sato, N. Hata, M. Asagiri, T. Nakaya, T. Taniguchi, N. Tanaka, Positive feedback regulation of type I IFN genes by the IFN-inducible transcription factor IRF-7, FEBS Lett. 441 (1998) 106–110.

[25] I. Marie, J.E. Durbin, D.E. Levy, Differential viral induction of distinct interferon-α genes by positive feedback through interferon regulatory factor-7, EMBO J. 17 (1998) 6660–6669.

[26] T. Taniguchi, A. Takaoka, The interferon α/β system in antiviral responses: a multimodal machinery of gene regulatory by the IRF family of transcription factors, Curr. Opin. Immunol. 14 (2002) 111–116.

[27] S.J. Haque, B.R. Williams, Identification and characterization of an interferon (IFN)-stimulated response element-IFN-stimulated gene factor 3-independent signaling pathway for IFN-α, J. Biol. Chem. 269 (1994) 19523–19529.

[28] J.E. Darnell, I.M. Kerr, G.R. Stark, Jak-stat pathways and transcriptional activation in response to IFNs and other extracellular signaling proteins, Sci. 264 (1994) 1415–1421.

[29] K. Honda, H. Yanai, H. Negishi, M. Asagiri, M. Sato, T. Mizutani, N. Shimada, Y. Ohba, A. Takaoka, N. Yoshida, T. Taniguchi, IRF-7 is the master regulator of type-I interferon-dependent immune responses, Nat. 434 (2005) 772–777.

[30] M. Sato, H. Suemori, N. Hata, M. Asagiri, K. Ogasawara, K. Nakao, T. Nakaya, M. Katsuki, S. Noguchi, N. Tanaka, T. Taniguchi, Distinct and essential roles of transcription factors IRF-3 and IRF-7 in response to viruses for IFN-alpha/beta gene induction, Immunity 13 (2000) 539–548.

[31] Y. Li, C. Li, P. Xue, B. Zhong, A.P. Mao, Y. Ran, H. Chen, Y. Wang, F. Yang, H. Shu, ISG56 is a negative-feedback regulator of virus-triggered signaling and cellular antiviral response, Proc. Natl. Acad. Sci. USA 106 (2009) 7945–7950, doi:10.1073/pnas.0900818106.

[32] X. Wang, S. Hussain, E.J. Wang, M.O. Li, A. Garcia-Sastre, A.A. Beg, Lack of essential role of NF-κB p50, RelA, and cRel subunits in virus-induced type 1 IFN expression, J. Immunol. 178 (2007) 6770–6776.

[33] E. Klipp, W. Liebermeister, C. Wierling, A. Kowald, H. Lehrach, R. Herwig, Systems Biology: A Textbook, Wiley-VCH, 2009.

[34] Z. Szallasi, J. Stelling, V. Periwal, System Modeling in Cell Biology: From Concepts to Nuts and Bolts, The MIT Press, 2006, pp. 97–105.

[35] U. Alon, An Introduction to Systems Biology Design Principles of Biological Circuits, Chapman Hall CRC, 2006.

[36] S.I. Bazhan, O.E. Belova, Interferon-induced antiviral resistance. A mathematical Model of Regulation of Mx1 Protein Induction and Acton, J. Theor. Biol. 198 (1999) 375–393.

[37] T. Tian, K. Burrage, Stochastic models for regulatory networks of the genetic toggle switch, Proc. Natl. Acad. Sci. (USA). 103 (2006) 8372–8377.

[38] D.T. Gillespie, Exact stochastic simulation of coupled chemical reactions, J. Phys. Chem. 81 (1977) 2340–2361, doi:10.1021/j100540a008.

[39] C. Rao, A. Arkin, Stochastic chemical kinetics and the quasi steady-state assumption: application to the Gillespie algorithm, J. Chem. Phys. 118 (2003) 4999–5010.

[40] P. Thomas, A.V. Straube, R. Grima, The slow-scale linear noise approximation: an accurate, reduced stochastic description of biochemical networks under timescale separation conditions, BMC Syst. Biol. 6 (2012) 39.

[41] S. Schnell, Validity of the Michaelis-Menten equation - steady-state or reactant stationary assumption: That is the question, FEBS J 281 (2) (2014) 464–472.

[42] R. Grima, P. Thomas, A.V. Straube, How accurate are the nonlinear chemical Fokker-Planck and chemical Langevin equations? J. Chem. Phys. 135 (8) (2011) 084103.

[43] S.M. Hanson, S. Schnell, Reactant stationary approximation in enzyme kinetics, J. Phys. Chem. A 112 (37) (2008) 8654–8658.

[44] D.J. Higham, Modeling and simulating chemical reactions, SIAM Rev. 50 (2008) 347–368, doi:10.1137/060666457.

[45] B. Ermentrout, Simulating, Analyzing, and Animating Dynamical Systems: A Guide to XPPAUT for Researchers and Students, SIAM, Philadelphia, 2004.

[46] OSCILL8, Available online: http://oscill8.sourceforge.net/ (accessed on 3 April 2013).

[47] M. Han, S. Gu, Theory and Method of Nonlinear System, Science Press, Beijing, China, 2001.

[48] K. Burrage, P.M. Burrage, T. Tian, Numerical methods for strong solutions of stochastic differential equations: an overview, Proc. Royal Soc. London A 460 (2004) 373–402.

[49] K.S. Kobayashi, R.A. Flavell, Shielding the double-edged sword:negative regulation of the innate immune system, J. Leukoc. Biol. 75 (2004) 428–433.

[50] F.Y. Liew, D. Xu, E.K. Brint, L.A. O'Neill, Negative regulation of toll like receptor-mediated immune responses, Nat. Rev. Immunol. 5 (2005) 446–458.

[51] P. Hänggi, H. Grabert, P. Talkner, H. Thomas, Bistable systems: Master equation versus Fokker-Planck modelling, Phys. Rev. A. 29 (1) (1984) 371–378.

[52] U. Rand, M. Rinas, J. Schwerk, G. Nöhren, M. Linnes, A. Kröger, M. Flossdorf, K. Kály-Kullai, H. Hauser, T. Höfer, M. Köster, Multi-layered stochasticity and paracrine signal propagation shape the type-I interferon response, Mol. Syst. Biol. 8 (2012) 584.

[53] E. Ford, D. Thanos, The transcriptional code of human IFN-beta gene expression, Biochim. Biophys. Acta. 1799 (2010) 328–336.

[54] M.B. Elowitz, A.J. Levine, E.D. Siggia, P.S. Swain, Stochastic gene expression in a single cell, Sci. 297 (2002) 1183–1186.

[55] Y. Li, M. Yi, X. Zou, The linear interplay of intrinsic and extrinsic noises ensures a high accuracy of cell fate selection in budding yeast, Scientific Rep. 4 (2014) 5764, doi:10.1038/srep05764.

[56] B. Snijder, L. Pelkmans, Origins of regulated cell-to-cell variability, Nat. Rev. Mol. Cell. Biol. 12 (2011) 119–125.

[57] P. Thomas, N. Popovic, R. Grima, Phenotypic switching in gene regulatory networks, Proc. Natl. Acad. Sci. USA 111 (19) (2014) 6994–6999.

[58] L. Cantini, C. Cianci, D. Fanelli, E. Massi, L. Barletti, Linear noise approximation for stochastic oscillations of intracellular calcium, J. Theor. Biol. 349 (2014) 92–99.

[59] S. Rao, A. van der Schaft, K. van Eunen, B.M. Bakker, B. Jayawardhana, A model reduction method for biochemical reaction networks, BMC Syst Biol. 8 (2014) 52.

[60] H. Schmidt, M. Madsen, S. DanøS, G. Cedersund, Complexity reduction of biochemical rate expressions, Bioinform. 24 (2008) 848–854.

[61] X. Xiao, W. Zhang, X. Zou, A new asynchronous parallel algorithm for inferring large-scale gene regulatory networks, Plos one 10 (3) (2015) e0119294, doi:10.1371/journal.pone.0119294.

[62] Y. Eynaud, D. Nerini, M. Baklouti, J.C. Poggiale, Towards a simplification of models using regression trees, J. R. Soc. Interf. 10 (2013) 20120613.

[63] S. Marino, I.B. Hogue, C.J. Ray, D.E. Kirschner, A methodology for performing global uncertainty and sensitivity analysis in systems biology, J. Theor. Biol. 254 (1) (2008) 178–196.

[64] J.K. Kim, K. Josic, M.R. Bennett, The validity of quasi-steady-state approximations in discrete stochastic simulations, Biophys. J. 107 (2014) 783–793.

[65] J.R. Pomerening, Uncovering mechanisms of bistability in biological systems, Curr. Opin. Biotechnol. 19 (2008) 381–388.

[66] D. Siegal-Gaskins, M.K. Mejia-Guerra, G.D. Smith, E. Grotewold, Emergence of switch-like behavior in a large family of simple biochemical networks, PLoS Comput Biol. 7 (5) (2011) e1002039, doi:10.1371/journal.pcbi.1002039.

[67] E.M. Ozbudak, M. Thattai, H.N. Lim, B.I. Shraiman, A. van Oudenaarden, Multistability in the lactose utilization network of escherichia coli, Nat. 427 (2004) 737–740.

[68] A.V. Ratushny, R.A. Saleem, K. Sitko, S.A. Ramsey, J.D. Aitchison, Asymmetric positive feedback loops reliably control biological responses, Mol. Syst. Biol. 8 (2012) 577, doi:10.1038/msb.2012.10.